Dynamic analysis of the Empact CVT : ratio and slip dependent, non-minimum phase dynamics

Dynamic analysis of the Empact CVT
Ratio and slip dependent, non-minimum phase dynamics

T.W.G.L. Klaassen, B.G. Vroemen and M. Steinbuch
Eindhoven University of Technology, Department of Mechanical Engineering
P.O. Box 513, 5600MB Eindhoven, The Netherlands

Abstract

The dynamics of an electromechanically actuated metal V-belt (Empact) CVT is analyzed by studying a simplified linear model of the actuation system and a driveline model which includes the slip dynamics of the variator. The actuation system shows several CVT ratio depending modes. Linearization of the slip dynamics shows that the location and, moreover, the damping of the modes depends significantly on the amount of slip in the variator. Using pole-zero locations of the system it is shown that due to high overclamping a coupling between the primary and secondary side of the variator occurs with very large damping and due to underclamping the input and output sides of the variator are decoupled with low or even negative damping, resulting in an unstable system. Furthermore non-minimum phase behavior of the actuation is described. Using identification results from a non-linear model of the Empact CVT the interaction of the actuation and driveline dynamics is analyzed. Finally, measurements on a prototype of the Empact show similar behavior, however with very large damping of all of the modes.

1 Introduction

The pulleys of a pushbelt or chain type CVT are actuated axially to adjust transmission ratio and to apply slip-preventing belt clamping force. In conventional CVTs this is done using hydraulics. Hydraulic losses are however substantial. To reduce the energy consumption, an electromechanically actuated CVT is developed [6], also referred to as the Empact CVT. By using a double epicyclic gear system and a screw mechanism at both shafts of the CVT (figure 1), it is possible to actuate the metal V-belt CVT with two servomotors at the fixed world. That means that the rotation of the servomotors is decoupled from the rotation of the input and output shaft of the CVT. By rotating the primary servomotor, a relative rotation between the two sun gears of the epicyclic sets is realized. This results in a translation of the spindles at both pulleys. At the secondary side, by adjusting the torque delivered by the secondary servomotor,

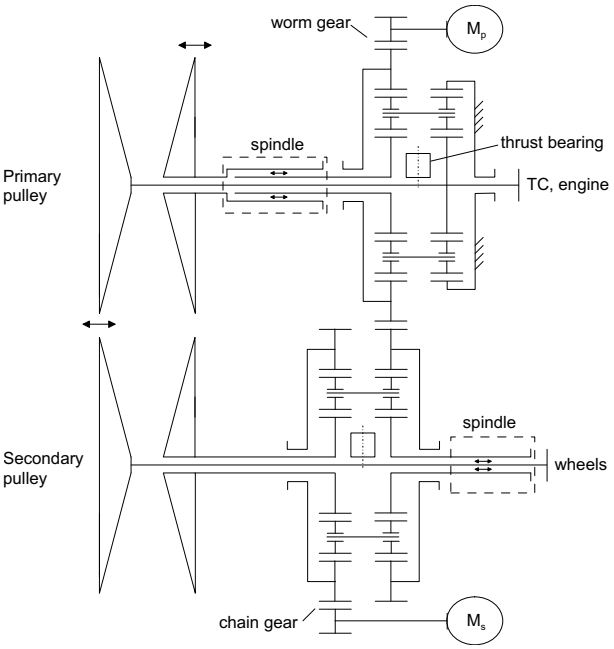

Figure 1: Electro-mechanically actuated CVT

the clamping force in the variator can be set and controlled. This system has the advantage that only mechanical power is needed when the CVT is shifting or when the clamping force is changed. The energy losses are reduced to a minimum in this way.

For analysis, control design and testing of the Empact CVT, a simulation model is built. This model is described in [4]. Due to its complexity and nonlinear behavior, this model is not suitable for control design. To use modern control design techniques like μ-synthesis, linear transfer functions from all inputs to all outputs must be known. Klaassen et al. [3] presents the identification of a linearized model from the non-linear simulation model using approximate realization techniques.

This paper first gives a dynamical analysis of the Empact CVT by studying the modes of the actuation system and the driveline separately. Furthermore non-minimum phase behavior of the system will be described. The interaction of these dynamics are described using identification results from a non-linear model of the Empact CVT in section 3. Finally to validate the analytic model, results from identification measurements will be shown.

2 Dynamic analysis

The model described in [4] includes all major driveline components and the electromechanically actuated CVT. A detailed model of the variator is implemented, which gives an accurate estimation of the clamping forces and slip in the system. In this model the worm gear with its

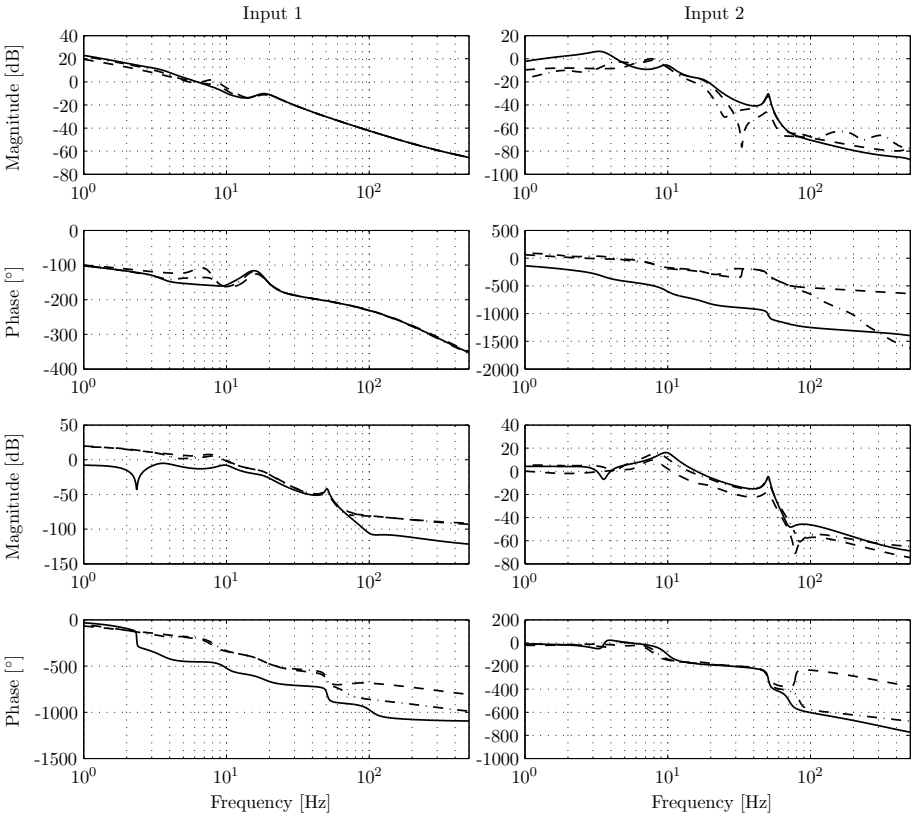

Figure 2: Transfer function from T_{mp} (Input 1) and T_{ms} (Input 2) to r_g (Output 1) and ν (Output 2) at $r_g = 0.5$ (-), $r_g = 1$ (- -) and $r_g = 2$ (-.)

bearing support, the chain at the secondary actuation and the thrust bearings, which support the axial force between the sun gears of the epicyclic gears at the primary and secondary side, are modeled as spring elements. As described in [3] and [1], the controlled variables are the geometric ratio r_g and the slip ν in the variator. The control inputs are the primary and secondary servo torque, T_{mp} and T_{ms} respectively. Linearization of the nonlinear model from these inputs to the outputs using approximate realization from step responses result in slip and ratio dependent transfer functions [3]. Figure 2 shows the transfer functions at ratio low, medium and overdrive. To get more insight in the resonances visible in the transfers function, the system is divided into two parts, i.e. a linear model for the actuation system and a model for the driveline, in this case the testbench. Furthermore non-minimum phase behavior resulting from the geometry of the variator will be described.

2.1 Actuation system

The first part is a linear, lumped parameter representation of the actuation system as shown in figure 3. In this model the pushbelt is represented as a flexible element. The stiffness of this element is the longitudinal stiffness of the steel bands of the pushbelt, combined with the stiffness of the pushing segments on the tense side. The thrust bearings are modeled as translational springs which support the screw output in longitudinal direction. The worm is represented as a rotational spring between the output of the worm and the ring gear of the epicyclic gear at the primary side. Finally the chain which connects the secondary servo to the ring gear of the epicyclic set is modeled as a flexible element. All flexible elements are subjected to proportional damping. Other non-conservative forces that act on the system are viscous friction in both servos and screws and a damping force that acts on the pulleys according to Shafai's model [5].

The epicyclic sets are modeled as a normal gear with a ratio of 2, which is the ring to sun ratio. The carriers and planets of the epicyclic sets are not modeled as separate bodies, but their inertias are combined with the ring inertia. The screws make the connection from the translating to the rotating part by their kinematic relation $x_{in} - x_{out} = s\left(\theta_{in} - \theta_{out}\right)$ where x_{in} and x_{out} are the input (nut) and output (bolt) translations, θ_{in} and θ_{out} are the input and output rotations and s is the pitch. For clarity, the part of the screw that is connected to the corresponding pulley is called the output side. The inertias of the screws are combined with the inertias of the sun gears, whereas the mass of the output of the screw is combined with the mass of the pulley.

Using Lagrange's equations of motion a dynamic model can be derived for this system. Six generalized coordinates are required to describe the system, that is the rotation of the primary servo q_1, the rotation of the secondary servo q_2, the rotation of the primary sun gear at the output side of the screw q_3, the rotation of the secondary sun gear at the input side of the screw q_4, the translation of the primary pulley q_5 and the translation of the secondary pulley q_6. Note that by the coupling of the ring gear between the primary and secondary side, the rotation of the sun at the output side of the secondary screw can also be expressed as q_3. Furthermore, the translation of the input of the primary and secondary screw can be expressed as $q_7 = sq_3 + q_5$ and $q_8 = s\left(q_4 - q_3\right) + q_6$ respectively.

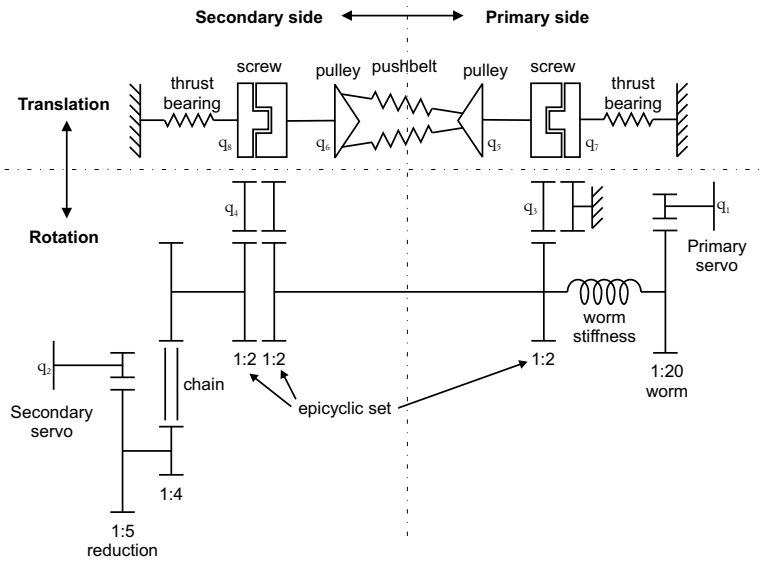

Figure 3: Linear representation of the actuation system

Undamped eigenmodes

By forming the mass matrix M and stiffness matrix K, the undamped eigenfrequencies f_r and corresponding eigenvectors can be calculated. The eigenfrequencies are listed in table 1. The eigenvectors are mass-normalized and normalized for the gear and screw ratios so that they all have the same order of magnitude. Figure 4 shows the eigenvectors for $r_g = 1$. Here also the normalized displacements of q_7 and q_8 are shown. For the sake of clarity, the high frequent modes are plotted in the right figure. Furthermore, figure 5 shows the normalized potential energy of the five spring elements in each mode. Here spring numbers 1 to 5 are the worm, chain, pushbelt, primary and secondary thrust bearing respectively. The sign of the energy shows whether the spring is elongated or shortened. From these two figures it is possible to see the influence of the bodies and springs on each mode. For matter of convenience, the normalized eigenvectors are referred to as displacements $\tilde{q}_{1-8}$.

As expected a rigid body mode is present, where $\tilde{q}_1$ to $\tilde{q}_6$ are equal and $\tilde{q}_7 = \tilde{q}_8 = 0$. The potential energy is of course zero here. The second eigenvector with $f_r = 10.7$ [Hz] originates from the worm stiffness in combination with belt and thrust bearings. In this case the rotation of $\tilde{q}_1$ and $\tilde{q}_3$ is in the same direction. The third mode at $f_r = 17.3$ shows similar behavior, but in this case $\tilde{q}_1$ and $\tilde{q}_3$ are opposite in direction. For the mode at $f_r = 47.9$ [Hz] it is clear that this originates from the chain at the secondary servo. The potential energy of the other elements are close to zero in this mode. The two translational modes are both at very high frequency. Mode number 5 is an in-phase translation of both pulleys, whereas mode 6 is an out of phase

Table 1: Undamped actuation eigenfequencies

	f_r [Hz]		
mode	$r_g = 0.5$	$r_g = 1$	$r_g = 2$
1	0	0	0
2	10.9	10.7	10.5
3	17.4	17.3	17.2
4	48.1	47.9	47.7
5	2.74 $\cdot 10^3$	2.74 $\cdot 10^3$	2.75 $\cdot 10^3$
6	3.93 $\cdot 10^3$	3.92 $\cdot 10^3$	3.91 $\cdot 10^3$

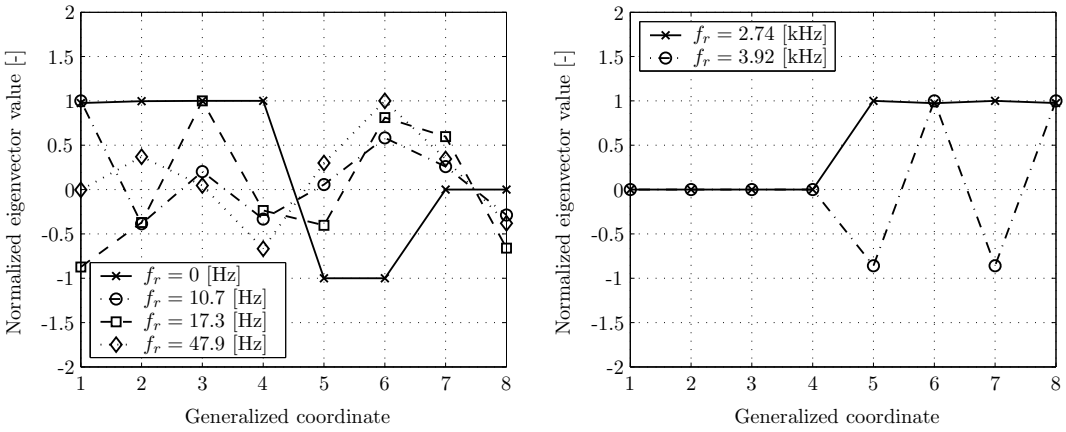

Figure 4: Undamped eigenvectors of the actuation model at $r_g = 1$

translation of the pulley. As can be seen from the potential energy in these modes, in mode 5 the pushbelt is not actuated, whereas in mode 6 the pushbelt is elongated.

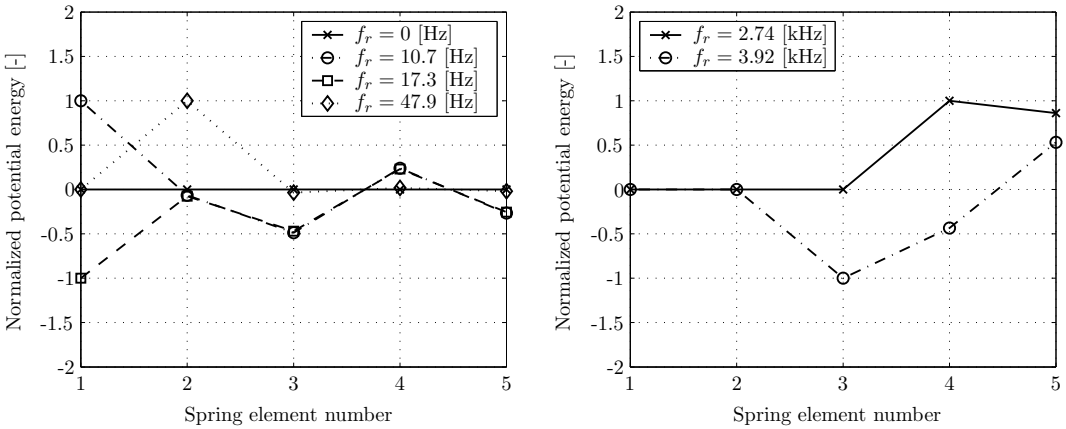

Figure 5: Normalized potential energy at $r_g = 1$

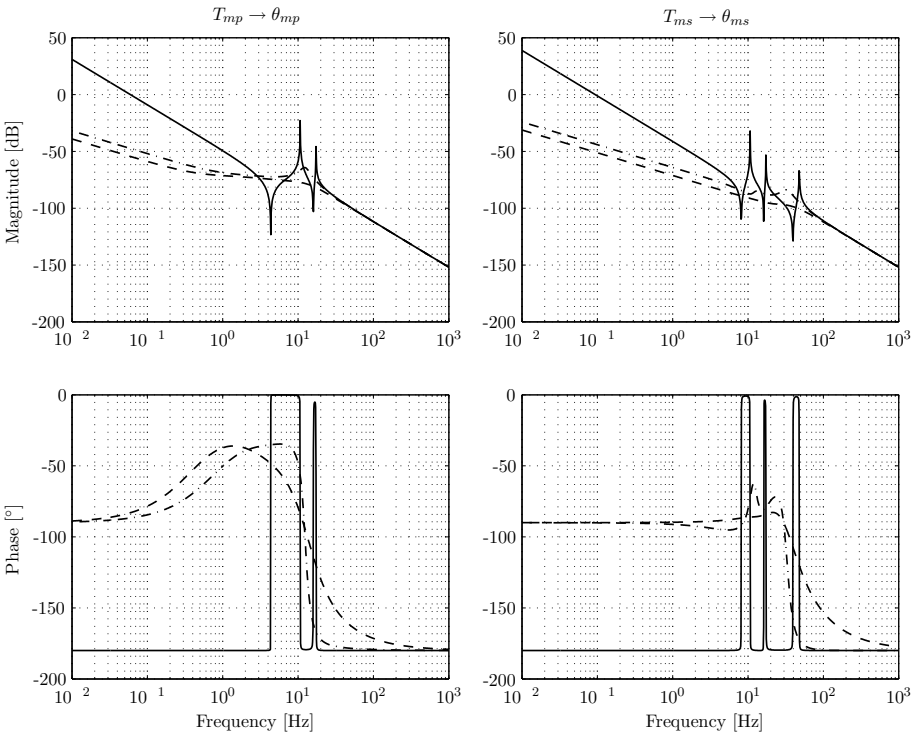

Figure 6: Transfer functions from servo torque to position, undamped (–), moderate damping (-.), and large damping (- -)

Damped eigenmodes

To determine the actual influence of each eigenmode, damping is added to the model. Figure 6 shows the transfer functions from primary servo torque T_{mp} to position $q_1 = \theta_{mp}$ and secondary servo torque T_{ms} to position $q_2 = \theta_{ms}$ with increasing damping. It can be seen that when adding damping (moderate damping), the resonances are smaller in magnitude and shift to lower frequencies. When adding large damping, most modes become invisible. For low frequencies both transfer functions now show a -1 slope and for high frequencies a -2 slope.

2.2 Driveline

The model of the driveline, in this case the testbench, is shown in figure 7. The torque converter lockup clutch is modeled as a rotational stiffness at the input shaft. The inertia of the torque converter is incorporated in the primary shaft of the CVT. The pushbelt is here modeled as a chain element with a certain rotational stiffness between the primary and secondary pulley. Furthermore, at the output of the CVT, the driveshaft is also modeled as a rotational stiffness. Note that this situation differs from that in a vehicle, because the inertias of the driving and load

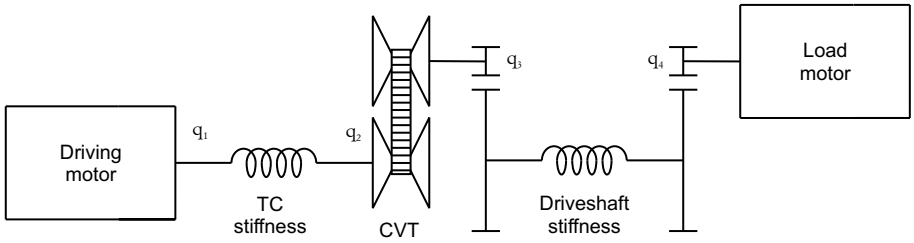

Figure 7: Schematic representation of the driveline

Table 2: Undamped driveline eigenfrequencies

	f_r [Hz]		
mode	$r_g = 0.5$	$r_g = 1$	$r_g = 2$
1	0	0	0
2	3.52	4.14	5.38
3	24.0	22.5	19.7
4	236	205	184

motor are different from the inertias in a vehicle.

The generalized coordinates are the angular rotation of the four bodies. Table 2 and figure 8 show the eigenfrequencies, normalized eigenvectors and normalized potential energy of the system. The first eigenmode is again a rigid body mode. The second mode at $f_r = 4.14$ [Hz] is mainly due to the driveshaft stiffness as can be seen from the potential energy plot. The third eigenmode at $f_r = 22.5$ [Hz] can be allocated to the torque converter stiffness. The last mode at relatively high frequency is due to the pushbelt stiffness.

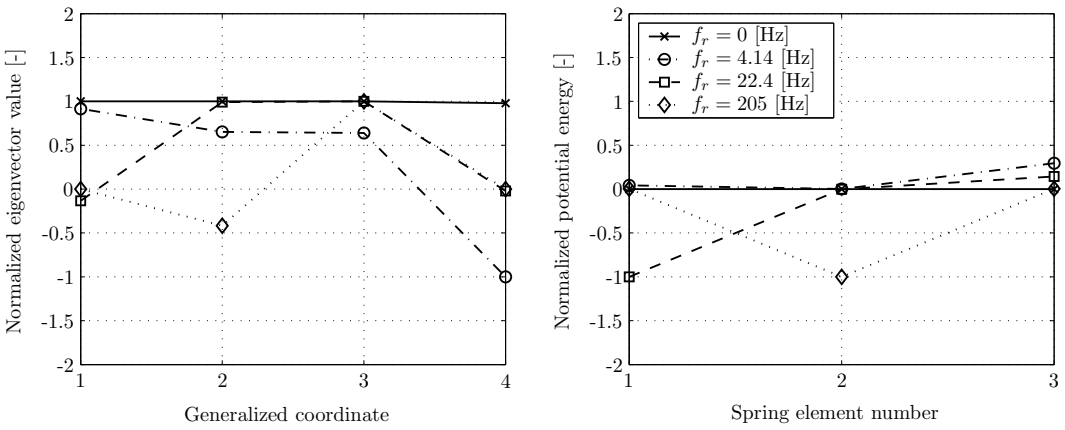

Figure 8: Undamped eigenvectors and potential energy at $r_g = 1$

Slip dynamics

If the pushbelt is modeled as a spring element like in the aforementioned model, by definition no slip would be present. However, if in the limiting case the pushbelt stiffness is zero, slip can be present. In practise, the coupling between the primary and secondary pulley is realized by the transmitted belt torque [2] given by

$$T_b = \frac{2\mu(\nu, r_g)F_s R_s}{\cos(\beta)} \tag{1}$$

where $\mu(\nu, r_g)$ is a slip and ratio dependent traction coefficient, F_s is the clamping force at the secondary pulley, R_s is the running radius of the belt on the secondary pulley and β is the pulley wedge angle. Slip in the variator is defined as

$$\nu = 1 - \frac{\omega_s R_s}{\omega_p R_p} \tag{2}$$

where $\omega_p = \dot{q}_2$ and $\omega_s = \dot{q}_3$ corresponding to the driveline model and R_p is the running radius of the belt on the primary pulley. The ratio $r_g = R_p/R_s$ is referred to as the geometric ratio.
If this belt torque is linearized with respect to the state vector $x = [q_1 \dots q_4 \ \dot{q}_1 \dots \dot{q}_4]^T$ and the input $u = F_s$, around a certain operating point $x = x_0 + \tilde{x}$ and $u = u_0 + \tilde{u}$ at a constant geometric ratio r_g, this results in

$$\bar{T_b} = \frac{2\mu'(\nu_0, r_g)u_0 R_p}{\dot{q}_{20}\cos(\beta) r_g}\left(\frac{\dot{q}_{3_0}}{\dot{q}_{2_0}}\tilde{q}_2 - \tilde{\dot{q}}_3\right) + \frac{2\mu(\nu_0, r_g)R_s}{\cos(\beta)}\tilde{u} \tag{3}$$

where $\mu'(\nu_0, rg)$ is the slope of the traction curve at the corresponding slip value. Hence, the belt torque can be modeled as a linear damper with damping constant $c_b = \frac{2\mu'(\nu_0, r_g)F_{s_0}R_p}{\dot{q}_{20}\cos(\beta)r_g}$ [Ns/rad] between the primary and secondary pulley, i.e. between the generalized coordinates q_2 and q_3.
In case the damping constant of this damper is small, the primary and secondary side of the driveline are decoupled. In this situation two rigid body modes are present, one mode of the primary side at $f_r = 15.5$ [Hz] and one mode of the secondary side at $f_r = 24.6$ [Hz]. However, with increasing damping c_b coupling between the primary and secondary side occurs. Figure 9 shows the root locus of the system for increasing c_b. It can be seen that the damping of the complex pole pair at 15.5 [Hz] increases as it turns towards the real axis. At the real axis, one of these poles goes to $-\infty$, whereas the other goes towards 0. Due to increasing coupling between both shafts, one of the rigid body mode poles goes from 0 towards negative real values. At a certain point the two real poles become one complex conjugate pair. A further increase of

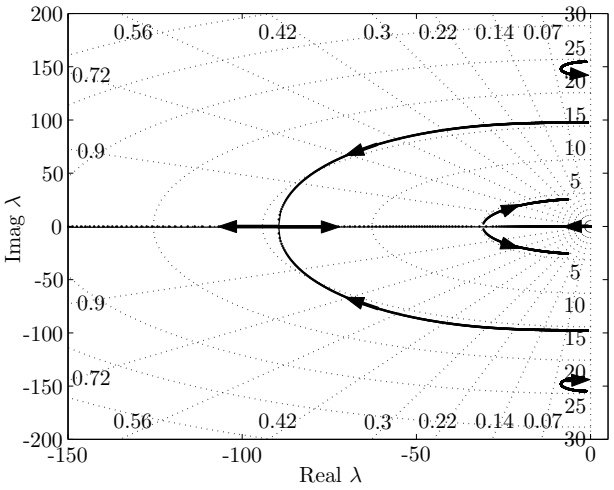

Figure 9: Root locus of driveline poles with increasing damping

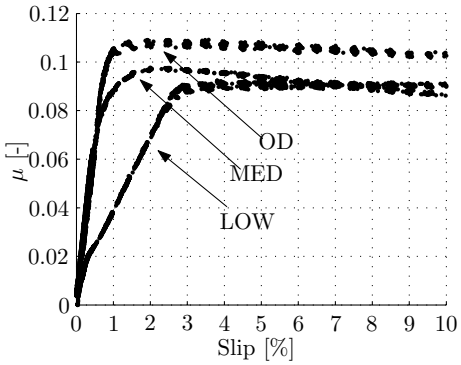

Figure 10: Traction coefficient μ at ratio $r_g = 0.43$ (LOW), $r_g = 1$ (MED) and $r_g = 2.25$ (OD)

the damping makes this pole pair turn towards the undamped eigenfrequency of the coupled system at $f_r = 4.14$ [Hz]. The primary and secondary side are fully coupled again. The last pole pair at 24.6 [Hz] turns to the undamped eigenfrequency $f_r = 22.5$ [Hz] as c_b increases.

The damping c_b depend significantly on the slope of the traction coefficient. Figure 10 shows μ at three different ratios. It can be seen that with increasing ν, μ also increases until a certain maximum value is reached. For higher slip values μ even shows a decrease at some ratios, resulting in a negative damping coefficient.

Figure 11 shows the poles of the model for increasing ν at $r_g = 1$, $F_{s_0} = 10$ [kN] and $\dot{q}_{2_0} = 300$ [rad/s]. It can be seen that the poles turn towards the imaginary axis for increasing ν or decreasing μ' (indicated by the arrows). This means that the damping of the corresponding pole decreases. When μ' becomes negative, some poles turn to the right half plane, indicating unstable behavior. The values of ν, F_{s_0} and $\dot{q}_{2_0}$ chosen here do not result in a strongly coupled system, as the resonance frequencies are close to the eigenfrequencies of the uncoupled sys-

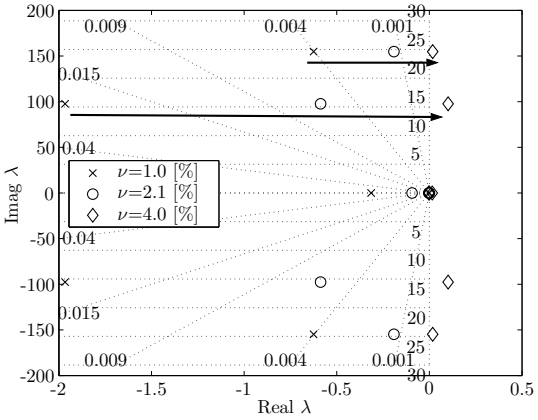

Figure 11: Pole locations of slip model for increasing ν

tem, however at higher clamping forces and lower angular velocities the damping increases such that the system becomes strongly coupled.

Figure 12(a) shows corresponding transfer functions from the clamping force F_s to the output of the system, that is the linearized slip $\bar{\nu} = \frac{1}{\dot{q}_{2_0} r_g} \left(\frac{\dot{q}_{3_0}}{\dot{q}_{2_0}} \tilde{\dot{q}}_2 - \tilde{\dot{q}}_3 \right)$. At $\nu = 0.1$ [%] the system is fully coupled. The system shows complete different behavior in this high overclamping situation. Both resonances clearly show a decrease of damping for an increase of ν. The phase plot shows again the unstable behavior at $\nu = 4.0$ [%], indicated by the increase of phase at both resonance frequencies. The figure shows also that two zeros are present in the transfer function. With the chosen input and output, the location of these zeros depend on the geometric ratio. Figure 12(b) shows the transfer function at different ratio, whereas figure 13 shows the root locus of the zeros with increasing ratio.

2.3 Non-minimum phase behavior

An important property of the variator is that, while shifting, the translation of the primary and secondary pulley are not equal. This is due to the fact that the wrapped angle of the pushbelt on the pulleys depends on the ratio. This angle can be expressed as

$$\varphi = \arcsin\left(\frac{R_p - R_s}{a}\right) \tag{4}$$

The translation of the pulley is a linear function of the running radius of the belt at the corresponding pulley, i.e. $x_{p,s} = (R_{p,s} - R_0)\tan(\beta)$. Hence, the difference in translation between both pulleys can be written as

$$\Delta_x = a \sin(\varphi) \tan(\beta) \tag{5}$$

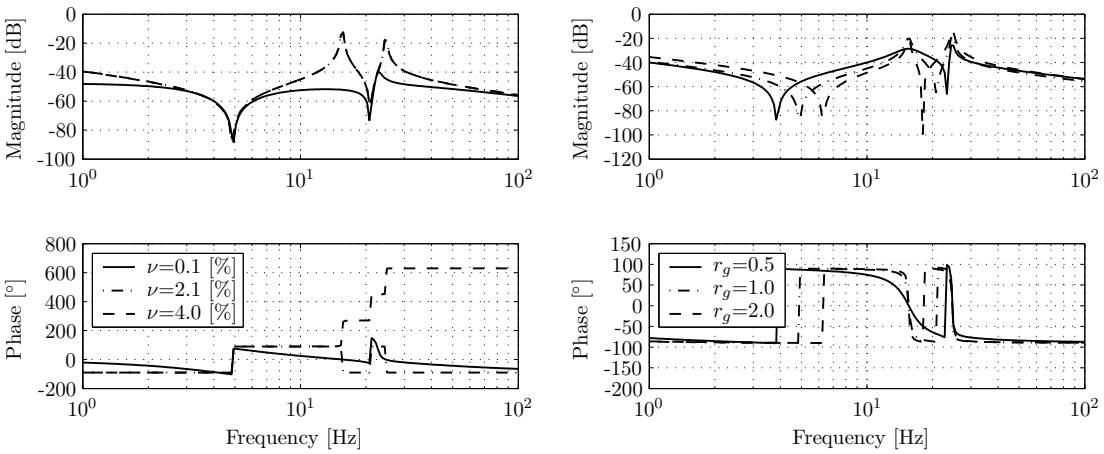

(a) $r_{g_0} = 1$ (b) $\nu_0 = 1$

Figure 12: Transfer function from F_s to $\tilde{\nu}$

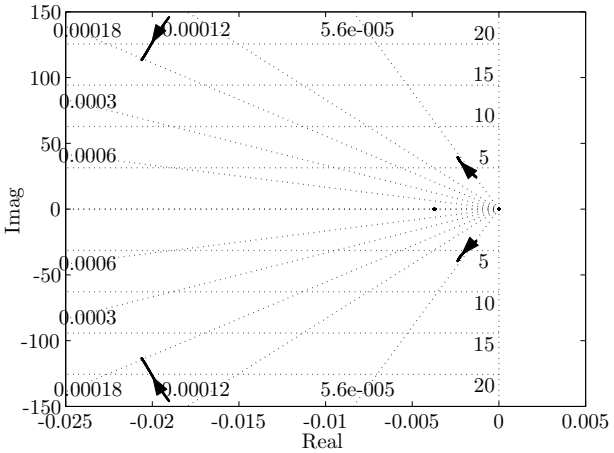

Figure 13: Root locus of the zeros of the slip model with increasing r_g

where $\Delta_x = x_p - x_s$. This means that if the variator shifts from low to medium ratio $\Delta_x > 0$, whereas for ratio shifts from medium to overdrive $\Delta_x < 0$.
The length of the pushbelt can be expressed as

$$L = 2a\cos(\varphi) + (\pi + 2\varphi)R_p + (\pi - 2\varphi)R_s \tag{6}$$

Now consider the situation when the secondary servo actuation position is constant. If the ratio is changed by means of only rotating the primary servo, the translation of both pulleys would be equal. However, when shifting from low to medium $\Delta_x > 0$. As a result the length of the belt decreases, and with that the clamping force in the system decreases and therefor the slip in the system would increase. If the ratio is changed from medium to overdrive, $\Delta_x < 0$, L and F_s increase and ν decreases. Of course when shifting from overdrive to low the opposite is true.
If a small ratio change is applied and a constant torque T_{ms} is applied at the secondary servo, the slip would first change as described above and then stabilize at a constant value. With respect to the transfer function from T_{mp} to ν, this phenomenon results in a minimum phase behavior if $\Delta_x > 0$, and in a non-minimum phase behavior if $\Delta_x < 0$.

3 Interaction of actuation and driveline

When changing the ratio or the slip in the CVT, also the belt torque is changed and the driveline modes are actuated. From the other side, if the load at the CVT is changed, the servomotors of the actuation system must counteract to these disturbances to control the ratio and the slip in the CVT. To get a complete understanding of the dynamics of the Empact CVT, this interaction between the actuation and the driveline dynamics must be analyzed. For this, the transfer functions of the linearized non-linear model (see figure 2) are used. It can be seen that both the modes of the actuation system and the modes of the driveline are present in the system. A few difference can be noticed. The first difference is that the damping in the nonlinear model is much larger than in the linear model, resulting in a large coupling between the modes. A second difference is that the zeros of the mode from the actuation model at $f_r = 48$ [Hz] are at a higher frequency than the poles of this mode. This zero appears to be non-minimum phase for $r_g = 0.5$ and minimum phase for $r_g = 2$ as explained in section 2.3. This also holds for zeros in other elements of system.

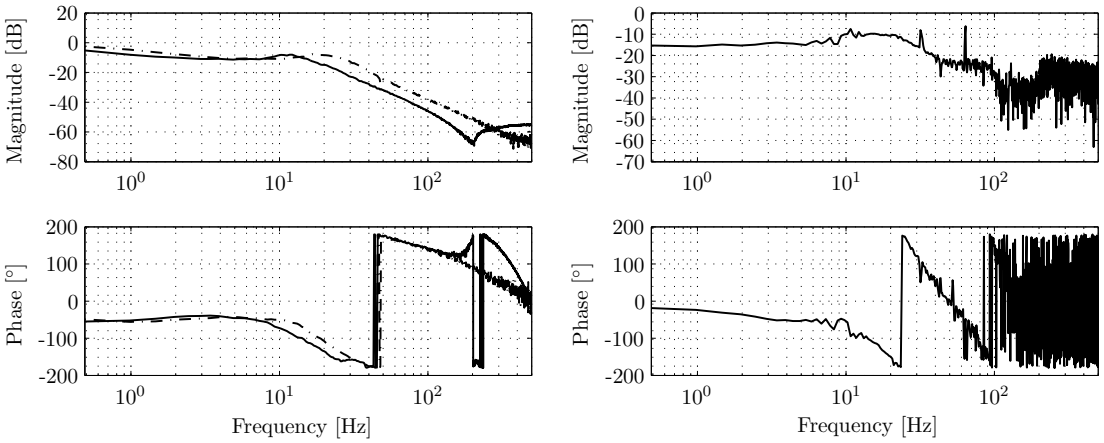

(a) FRF from T_{mp} to θ_{mp} and T_{ms} to θ_{ms} at $\nu_0 = 0\ \%$ and $r_g = 0.5$

(b) FRF from T_{ms} to θ_{ms} at $\nu_0 = 0\ \%$ and $r_g = 0.5$

Figure 14: Measured frequency response functions

4 Measured Frequency Response Functions

To validate the results obtained from the model, identification measurements are performed at a testrig. Figure 14 shows the measured frequency response functions from T_{mp} to θ_{mp}, T_{ms} to θ_{ms} and T_{ms} to ν. The measurement are strongly influenced by the friction in the CVT, mainly in the spindles of the actuation, but some conclusions can be drawn from these results.
As expected, the FRF from T_{mp} to θ_{mp} shows a -1 slope at low frequencies. The modes of the system are also strongly damped. The mass decoupling at the primary actuation is present, indicated by the phase increases between 2-6 [Hz] and the resonance at 13 [Hz]. Also between 40-50 [Hz] a small mass decoupling is present, probably due to the secondary actuator. The FRF from T_{ms} to θ_{ms} shows similar behavior, however with the first resonance around 20 [Hz]. The FRF from T_{ms} to ν shows similar behavior to the transfer function from the nonlinear model, however the disturbances on these measurement are too high and more measurements should be performed to obtain better results.

REFERENCES

[1] B. Bonsen, T.W.G.L. Klaassen, K.G.O. Van de Meerakker, P.A. Veenhuizen, and M. Steinbuch, *Analysis of slip in a continuously variable transmission*, Proceedings of Imece, no. 41360, 2003.

[2] T.W.G.L. Klaassen, B. Bonsen, K.G.O. van de Meerakker, M. Steinbuch, P.A. Veenhuizen, and F.E. Veldpaus, *Nonlinear stabilization of slip in a continuously variable transmission*, Proceedings of CCA (Taipei, Taiwan), 2004.

[3] T.W.G.L. Klaassen, B. Bonsen, K.G.O. van de Meerakker, B.G. Vroemen, and M. Steinbuch, *Control-oriented identification of an electromechanically actuated metal v-belt* CVT, Proceedings of CVHT (Davis, CA, USA), 2004.

[4] T.W.G.L. Klaassen, B.G. Vroemen, B. Bonsen, K.G.O. van de Meerakker, M. Steinbuch, and P.A. Veenhuizen, *Modelling and simulation of an electro-mechanically actuated push-belt type continuously variable transmission*, Proceedings of IFAC Mechatronics (Sydney, Australia), no. 95, 2004.

[5] E. Shafai, M. Simons, U. Neff, and H.P. Geering, *Model of a continuously variable transmission*, Proceedings of the 1st IFAC Workshop on Advances in Automotive Control, 1995, pp. 99 – 107.

[6] K.G.O van de Meerakker, P.C.J.N. Rosielle, B. Bonsen, T.W.G.L. Klaassen, and N.J.J. Liebrand, *Mechanism proposed for ratio and clamping force control in a* CVT, Proceedings of Fisita, no. F2004F108, 2004.